Research on Fault-Tolerant Control Strategy of Open-End Winding Drive With a Common DC Bus Under a Switch Open-Circuit Fault

Zhongjie ZOU, Shuying YANG, Yufeng ZHANG, and Xing ZHANG

***Abstract*—As the power core of a new energy vehicle, the operation reliability, especially the fault-tolerant operation ability of the electric drive system is directly related with the safety and user experience. The open-end winding topology with a common DC bus demonstrates many advantages and consequently attracts lots of attentions in the application of the new energy vehicles. However, most of existing fault-tolerant solutions for this topology, treat switch open-circuit fault as an open-circuit phase fault, which limits the system's fault-tolerant operation performance. Based on the analysis of the phase current and voltage characteristics after the switch open circuit fault, a fault-tolerant control scheme through biasing the fault-phase current is proposed in this paper, aiming to enhancing the load capability. Through this bias control the fault-phase current is only at one direction, i.e., positive or negative direction as expected, which allows the anti-parallel diode of the open-circuit switch be used to generate the voltage level desired. Therefore, the output voltage is not affected by the fault switch device. As found through mathematical calculation, both the output voltage and the output torque are increased greatly through the proposed fault tolerant scheme. At last, the effectiveness and advantages of proposed scheme is confirmed and demonstrated through experiments.**

***Index Terms*—Fault-phase current bias, fault-tolerant control, open-end winding topology, switch open-circuit fault.**

I. Introduction

THE open-end winding electric machine (OWEM) is formed by opening the neutral point of the stator winding of the traditional three-phase machine and supplying power from both ends of the windings with two inverters. Compared with the conventional driving system driven by one inverter, OWEM has many advantages such as multi-level voltage output capability, high DC voltage utilization, wide speed operation, and high fault-tolerant performance [1]. Therefore, the topology has been extensively researched in the past decade.

Manuscript received December 25, 2023; revised February 25, 2024; accepted March 12, 2024. Date of publication June 30, 2024; date of current version March 26, 2024. This work was supported by National Natural Science Foundation of China under Grant 51877062. *(Corresponding author: Shuying Yang.)*

All authors are with Hefei University of Technology, Hefei 230009, China (e-mail: zouzhongjie0927@163.com; yangsy@hfut.edu.cn; zyf_upc@163.com; honglf@ustc.edu.cn).

Digital Object Identifier 10.24295/CPSSTPEA.2024.00005

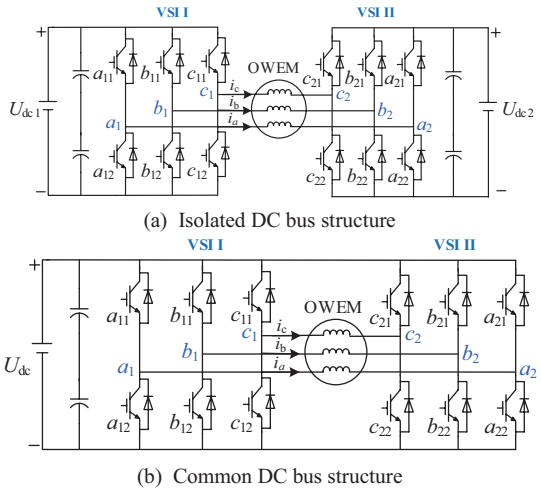

(a) Isolated DC bus structure

(b) Common DC bus structure

Fig. 1. Topology of OWEM.

According to the assignment of the DC buses of the dual inverters, this drive can be divided into that with isolated DC buses and that with a common DC bus, as shown in Fig. 1. Compared with that with isolated DC buses, the OWEM drive with a common DC bus only needs a set of DC bus to supply power, which simplifies the design of the power supply and reduces the cost and volume of the system. In addition, the structure of the common DC bus breaks the constraint that the sum of the three-phase stator currents is zero, which introduces an additional degree of freedom to the fault-tolerant control [2], beneficial to the improvement of fault-tolerant performance. Considering above advantages, the OWEM system with a common DC bus is more suitable to the new energy vehicle applications.

In recent years, with the popularity of the new energy vehicles, the reliability of electric drives has become the focus of attention [3]. As a relatively fragile link in the electric drive system, the power switching device has a high probability of failure [4]. Once a fault occurs, it is likely to cause safety accidents and increase operation and maintenance costs. To improve the reliability of the electric drive system, the switch fault diagnosis technology and the corresponding fault-tolerant operation scheme have become a popular research issue. After years of development, the related research on switch fault diagnosis technology [4]–[8] has matured comparatively,

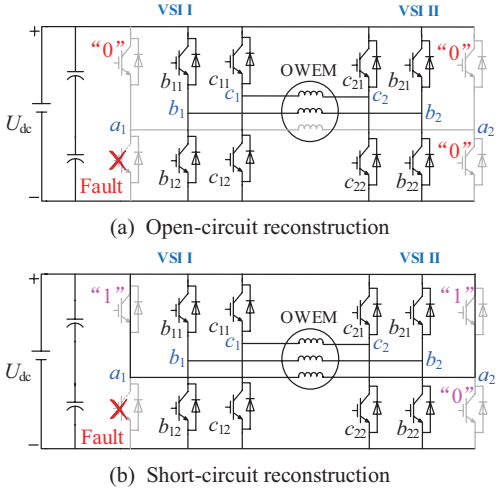

(a) Open-circuit reconstruction

(b) Short-circuit reconstruction

Fig. 2. Implementation method of two-phase operation.

but the fault-tolerant control after a switch fault is limited by the converter topology and has not been effectively solved. Compared with the traditional single-inverter electric drive system, the dual-inverter powered OWEM system itself has strong redundancy capability, which has inherent advantages in fault-tolerant operation. There are also many reports on the fault-tolerant operation scheme after a switch open-circuit fault of the OWEM system with a common DC bus.

Due to the existence of the zero-sequence circuit, after a switch fault occurrence in the OWEM system with a common DC bus, the fault-phase winding can be short-circuited or open-circuited by setting the remaining switches of the fault phase at often open or often closed states [9], [10], as demonstrated in Fig. 2, and the machine is operated with the remaining two-phase windings, i.e., operating in a two-phase mode. In [11], after isolating the fault-phase winding, the vector control method is used to achieve the fault-tolerant operation with two phases. The control method itself is too complicated to practice application. In [12], a unified SVPWM fault-tolerant control algorithm based on voltage vector decoupling control is proposed according to the distribution law of residual voltage vectors of dual inverters in the case of open-circuit phase fault. However, the fault-tolerant operation scheme needs to readjust the voltage vector, and the stator current is obviously distorted. To achieve an ideal current waveform in the non-fault phases, SPWM is used to control the two-phase converter in [13]. However, the scheme only improves the modulation strategy, and does not match the suitable control strategy. The torque still has obvious fluctuations. Based on the zero-sequence current injection operation, a direct torque tolerant control scheme for switching device under triggered suppression is proposed in [14], so that the same voltage vector range as before the fault can be obtained. But in essence, the machine is still operated in two-phase mode.

Although the two-phase fault-tolerant operation can be easily operated after many year researches, the torque capability is reduced too much. Consequently, in some cases the vehicle cannot be moved with the low torque. That is to say, the two-phase mode fault tolerant operation is not very applicable to vehicle applications. In order to increase the load capability of the machine, three phases should be used even after a switch fault. Combining with impedance source network and a 3-H bridge two-level inverter, the open-winding electric drive system with single-stage boosting and fault-tolerance function is proposed in [15], and the fault-tolerant is realized by adjusting the insertion time of the remaining shoot-through zero vector, but the scheme requires accessory hardware, which increases the cost and volume. In [16], the bridge arm sharing scheme is used to achieve fault-tolerant operation and to improve the torque capacity, but the current between each bridge arm is not balanced after the fault, limiting the torque, and the scheme also requires additional devices to reorganize the winding connection mode. In addition, two zero-sequence current injection modes are proposed in [17] to realize three-phase operation after switch or diode fault. However, the mode 1 scheme is only discussed in the case of diode open-circuit fault, which can not be directly applied to switch failure. Although the mode 2 scheme can realize the three-phase operation after one or even multiple switch failure, the torque capacity is not effectively improved compared with the continuous two-phase operation.

From the above reports, one can find that most of the existing fault-tolerant control schemes for this OWEM drive with a common DC bus treat one switch open-circuit fault equally as one phase open-circuit fault, and operate the machine in the two-phase mode, resulting in a significant decrease in torque output capacity. The fault-tolerant operation schemes using three phases require additional hardware devices, sacrificing its competitiveness in terms of cost, volume, and quality. In this paper, a fault-tolerant scheme operating the machine in three-phase mode but without additional hardware is proposed for one switch open-circuit fault of the OWEM system with a common DC bus. The research shows that compared with the continuous two-phase fault-tolerant scheme, the proposed scheme has higher voltage output capability and greater torque output capability, which lays a foundation for the improvement of fault-tolerant operation performance. Section II simply reviews the vector control system of the drive system in normal state. In Section III, a fault-tolerant control strategy is proposed based on the analysis of the current and voltage characteristics in the fault phase under a switch open-circuit fault. Also in this section, the linear modulation range of the proposed scheme is discussed, and the allowed torque and voltage are calculated and compared with the continuous two-phase mode operation. In Section IV, experimental results are presented to validate the proposed fault-tolerant control method. Finally, this article is summarized in Section V.

II. Vector Control System

The OWEM system with a common DC bus studied in this article is shown in Fig. 1(b), where U_{dc} is the DC bus voltage. Define the switching function $S_{mx} = 0$ or 1 (m = a, b, c, d; x = 1, 2) to represent the switch state of the bridge arm, i.e., "1" represents the conduction of the upper bridge arm, and "0" represents the conduction of the lower bridge arm. The phase

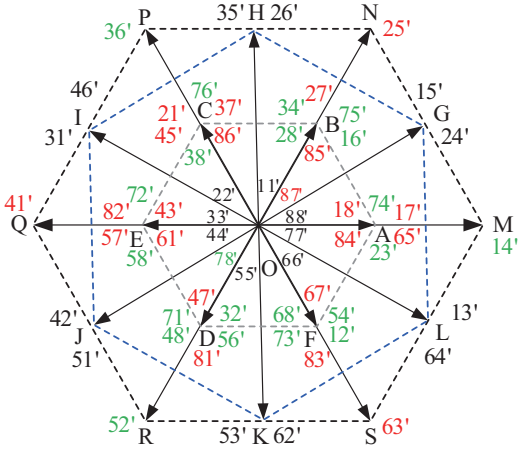

Fig. 3. Space voltage vector diagram of dual inverter.

voltages can be expressed as:

$$u_{mx} = S_{mx}U_{dc} \tag{1}$$

Consequently, the output voltage vector of a inverter can be expressed as:

$$\vec{u}_s = \frac{2}{3}(u_a + u_b e^{j2\pi/3} + u_c e^{j4\pi/3}) \tag{2}$$

Combining the switching states of the two inverters, 64 switching states can be produced of the open-end winding system, and the corresponding voltage vector distribution is shown in Fig. 3. According to the amplitudes of the voltage vectors, they can be divided into large voltage vectors (MNPQRS) with the amplitude of $4U_{dc}/3$, middle voltage vectors (GHIJKL) with the amplitude of $2\sqrt{3}U_{dc}/3$, small voltage vectors (ABCDEF) with the amplitude of $2U_{dc}/3$, and zero voltage vectors (O). For these voltage vectors, the corresponding zero-sequence voltages (ZSVs) may be positive marked in red, negative marked in green or zero marked in black.

The voltage vector required for vector control system of the open-end winding machine is generated by these two inverters with equal distribution. Common mode voltage (CMV) exists in the AC output of a single inverter is due to the PWM strategy and unideal factors such as dead-time effect, and device voltage drop [18], etc. The difference between the CMVs of these two inverters together with the zero-sequence component of the machine electromotive force form the ZSV in the zero-sequence loop. If without proper manipulation, zero-sequence current (ZSC) would appear. The ZSC can be controlled or sustained through actively controlling the ZSV component produced by the PWM action. A ZSC hysteresis control was presented in [19], where the suppression is achieved by choosing the switching combinations with the polarity of ZSV opposite to the ZSC polarity. The control scheme is simple and effective. Therefore, it is used in this article to control the ZSC in healthy state. The OWEM itself is controlled with space vector scheme. The overall control scheme is given in Fig. 4.

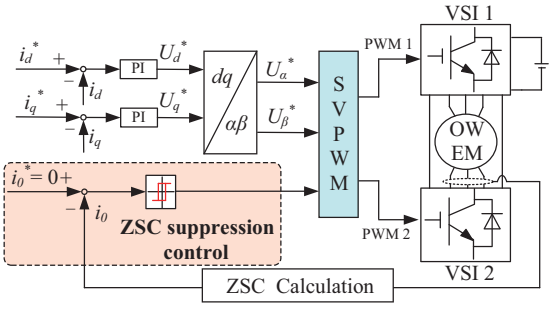

Fig. 4. Vector control system in healthy state.

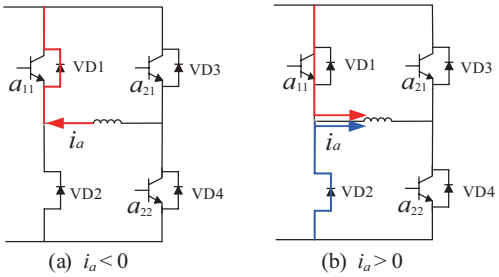

Fig. 5. i_a flow paths under a_{12} open-circuit fault.

III. Proposed Fault-Tolerant Control Strategy

A. Current Loops After a Switch Open-Circuit Fault

After a switch open-circuit fault, the stator current waveforms will be distorted due to some of the required voltage vectors cannot be generated. In the following, switch a_{12} will be taken as an example to make analysis of the possible current loops. When $S_{a1} = 0$, i.e., the fault bridge arm is command to conduct, a_{12} cannot conduct effectively due to the open-circuit fault. As a result, VSI 1 cannot ensure the output desired voltage u_{a1}. For the OWEM, a phase voltage is equal to the difference between the AC outputs of the bridges in this phase of the two inverters. According to the definition of the switching function, the switching function pair (S_{a1}, S_{a2}) can be equal to four possible combinations (0,0), (0,1), (1,0) and (1,1). a_{12} fault will affect the two combinations, (0,0) and (0,1). After the fault, the possible flow paths of phase-A current i_a in VSI 1 are shown in Fig. 5. Defines the direction of the current flowing into VSI 1 as the negative direction, and flowing out of VSI 1 as the positive direction. As shown in Fig. 5, for the negative current, the current can only flow through the antiparallel diode of the switch a_{11}, due to the open-circuit fault of a_{12}. So the output AC voltage of VSI 1 in phase A is U_{dc}, rather the 0 required. That is to say, the required voltage cannot be produced, which causes the stator voltage affected and the stator current distorted. However, as demonstrate in Fig. 5(b), the paths of the positive current are not affected, namely the required voltage during the positive current period can be produced correctly. From Fig. 5(a), it can be easily found that the negative current is in the regenerative mode, lack of exciting source. So, the negative current would attenuate to and stay at zero. As a result, the

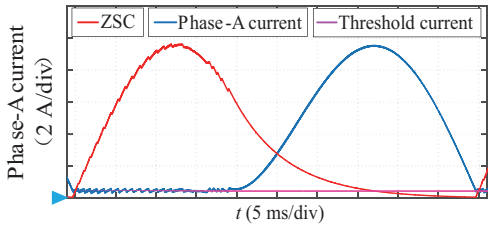

Fig. 6. Ideal phase-A current under bias control.

negative period of phase-A current is lost, the voltage vector range is in an unhealthy state in the negative half period [14], and if the normal control strategy is maintained, the command voltage vector will not be accurately synthesized during the period when the phase-A current is 0, and the system is in a faulty operation state.

To a machine, the ZSC would not affect the torque ideally. However, it can enforce effects on the phase current. If a proper ZSC current is injected, the current of the fault phase may flow only in one direction, as presented in [14] and [17]. However, in [14], the fault-phase current is biased at specific threshold throughout the fundamental period, which not only limits the selection range of voltage vectors, but also reduces the machine's load capacity. If the ZSC bias control is employed only in the half period when the phase current and phase voltage are affected, the system can achieve fault-tolerant operation with optimal performance. To Fig. 5 case, if the bias control is applied only in the negative half period to bias the phase-A current to positive instead of 0, then only positive current flow through phase-A winding, as shown in Fig. 5(b), the output voltage would not be affected by the fault switch. That is to say, the required voltage can be produced faithfully at any time instant. This property would be used to develop a fault-tolerant control strategy in this paper.

B. Fault-Tolerant Control Strategy

From the analysis of the previous section, one can find that to make the stator voltage unaffected during the fault operation, it is necessary to bias the fault-phase current to a proper direction. The bias is achieved through ZSC injection, and the bias control is enforced only for the necessary half period. Also taking a_{12} open-circuit fault as an example, to keep i_a always positive, a small positive threshold i_{th} is set to phase-A current. When $i_a > i_{th}$, there is no ZSC injection required, so during this period the ZSC is set equal to 0. Otherwise, once $i_a < i_{th}$ appears, the ZSC is increased as required. Ideally, phase-A current in a fundamental period is given in Fig. 6. Obviously, during the negative half period, phase-A current is maintained at the threshold value, while during the positive half period, it almost assumes the waveforms as that in healthy state. Therefore, with the proposed fault-tolerant control strategy, the machine operates in the two-phase and three-phase modes alternatively.

Different from the healthy operation, the ZSC is controlled as required by the fault-phase current during the fault-tolerant operation. The control scheme is demonstrated in Fig. 7.

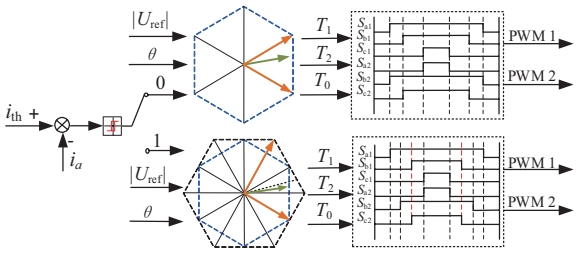

Fig. 7. The schematic diagram of CBFTC strategy.

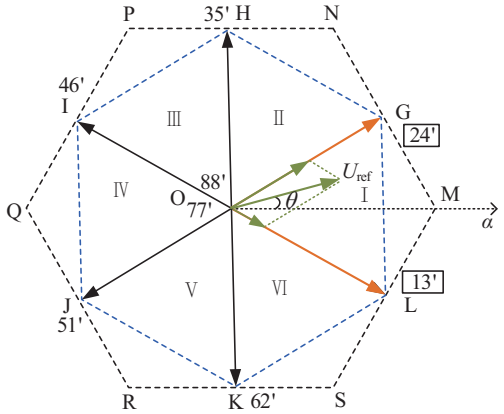

Fig. 8. Example diagram of basic voltage vector selection.

Instead of ZSC itself, phase-A current is used to control the ZSV and then the ZSC. If phase-A current is higher than the threshold, the required ZSC is 0. Therefore, the switching combinations with zero ZSV are selected. In this paper, the middle voltage vectors, as shown in Fig. 8, are used to generate the command voltage. Otherwise, the vectors with positive ZSV are used, aiming to generate the ZSC biasing phase-A current higher than the threshold. For presentation convenience, the proposed fault-tolerant control is named as a current-bias fault tolerant control (CBFTC).

Specifically, the CBFTC is presented as follows.

1) $i_a > i_{th}$

At this time, the expected ZSV is 0, and the voltage vectors with a zero ZSV, located on the middle hexagon GHIJKL in Fig. 8 are selected to generate the command voltage. It can be regarded as a specific voltage vector modulation strategy, presented in [20], [21]. Considering these middle voltage vectors as the basic voltage vectors, the $\alpha\beta$-plane is divided into six sectors. Taking the reference voltage vector located in the sector I as an example, the middle vector OL and OG are selected as the basic voltage vectors, and their active time T_1 and T_2 can be calculated respectively as:

$$\begin{cases} T_1 = \dfrac{2T_s|U_{ref}|}{\sqrt{3}|U_{13'}|}\cos(\theta - \dfrac{\pi}{3}) \\ T_2 = \dfrac{2T_s|U_{ref}|}{\sqrt{3}|U_{24'}|}\sin(\theta + \dfrac{\pi}{6}) \end{cases} \tag{3}$$

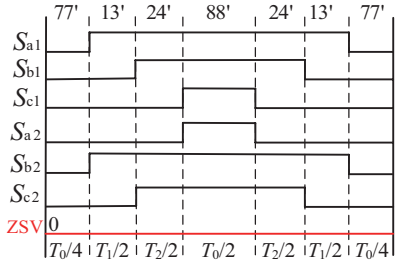

Fig. 9. Switching sequence pattern.

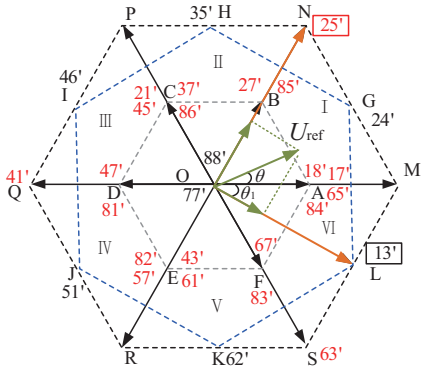

Fig. 10. Example diagram of basic voltage vector selection.

where $|U_{\text{refl}}|$, $|U_{13'}|$, $|U_{24'}|$ are the amplitude of the command voltage vector U_{ref} and the basic voltage vectors 13′, 24′, and θ is the phase angle of U_{ref}.

The switching sequence diagram combining the command voltage vector is shown in Fig. 9. The remaining time T_0 is divided equally by the two zero voltage vectors 77′ and 88′. It can be seen from Fig. 9 that the output ZSV of the PWM itself is always zero in a switching period. Therefore, the ZSC is not injected actively.

2) $i_a < i_{\text{th}}$

At this time, the expected ZSV is positive to inject the ZSC required to biasing phase-A current. Therefore, the switching combinations with positive ZSV on the small hexagon ABCDEF and on the large hexagon MNPQRS in Fig. 10 can be selected to generate the command voltage. Obviously, the $\alpha\beta$-plane is also divided into six sectors. In [19], to meet the modulation requirement of polar ZSVs while aiming for higher linear modulation range in the $\alpha\beta$-plane, a middle vector, a large vector with positive or negative ZSV and a zero vector are selected as the basic voltage vectors within each sector. Still taking the command voltage vector in sector I as an example, the middle vector OL and the large vector ON are selected for outputting positive ZSV instead of small vectors OA and OB, and their action times T_1 and T_2 can be calculated respectively as:

$$\begin{cases} T_1 = \dfrac{T_s|U_{\text{ref}}|}{|U_{13'}|}\cos(\theta + \dfrac{\pi}{6}) \\ T_2 = \dfrac{T_s|U_{\text{ref}}|}{|U_{25'}|}\sin(\theta + \dfrac{\pi}{6}) \end{cases} \tag{4}$$

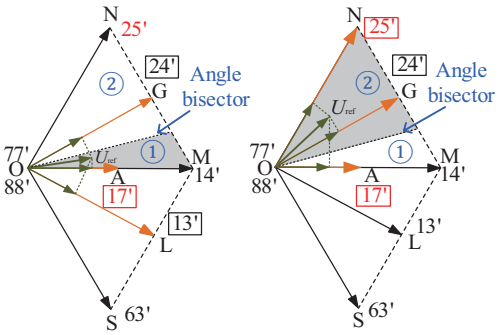

Fig. 11. Equivalent composite diagram of command voltage vector.

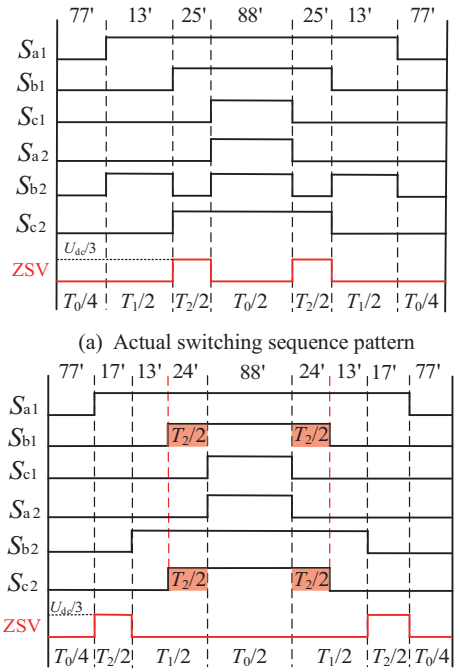

Fig. 12. Switching sequence pattern of sub-sector ① .

It can be found from (4) that when the command voltage vector is located on the angular bisector of the two basic voltage vectors, $T_1 = T_2$. To simplify the analysis, the sector I is further divided into two sub-sectors ① and ② with the angular bisector of OL and ON as the dividing line, which is shown in Fig. 11. When the command voltage vector is located in sub-sector ① , there is $T_1 > T_2$. At this time, the switching sequence diagram can be drawn in Fig. 12(a). Obviously, the bridge arm b_2 switching 6 times in one sampling period, which will undoubtedly increase the switching loss and is difficult to implementation. According to [19], the actual switching sequence can be equivalently replaced by the switching sequence shown in Fig. 12(b). As the conduction time of each switch for these two switching sequences remains unchanged, it will not affect generation of the command voltage vector. However, with the new switching sequence, the command voltage vector is equivalently synthesized with the basic vectors 13′, 17′ and

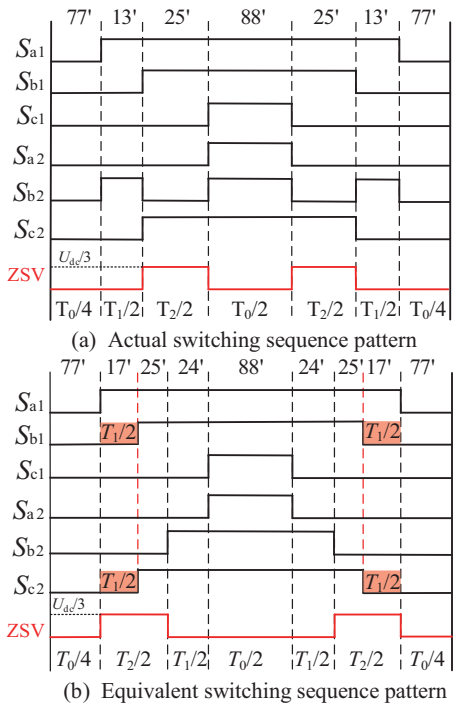

Fig. 13. Switching sequence pattern of sub-sector ② .

24′, as shown in Fig. 11(a). Comparing the ZSV output waveforms with these two switching combinations in Fig. 12(a) and (b), obviously the ZSV in voltage-second sense in one sampling period maintains unchanged with the new combination.

Similarly, when the command voltage vector is located in the sub-sector ② , $T_1 < T_2$. Again, to avoid multiple switching problems, the actual switching sequence shown in Fig. 13(a) is replaced by the equivalent switching sequence shown in Fig. 13(b), and the command voltage vector is equivalently synthesized with the vectors 17′, 24′ and 25′, as shown in Fig. 11(b).

Under the proposed fault-tolerant control strategy, the ideal three-phase current waveforms of the machine is shown in Fig. 14. Obviously, the machine is operated in the two-phase mode in the negative half cycle of i_a, and in three-phase mode in the positive half cycle of i_a. During the two-phase operation, to maintain the same torque output as the three-phase operation and avoid torque ripple, the amplitudes of the currents in the two healthy phases need to be increased to $\sqrt{3}$ times of that in the healthy state, and the phase difference is reduced from 2π/3 to π/3 [22]. Ignoring the influence of the smaller threshold current, the three-phase current after fault tolerance can be expressed as:

$$\begin{cases} i_a = I_m \sin\theta & 0 \leqslant \theta < \pi \\ i_b = I_m \sin(\theta - \frac{2}{3}\pi) & 0 \leqslant \theta < \pi \\ i_c = I_m \sin(\theta + \frac{2}{3}\pi) & 0 \leqslant \theta < \pi \\ i_a = i_{th} & \pi \leqslant \theta \leqslant 2\pi \\ i_b = \sqrt{3} I_m \sin(\theta - \frac{5}{6}\pi) & \pi \leqslant \theta \leqslant 2\pi \\ i_c = \sqrt{3} I_m \sin(\theta + \frac{5}{6}\pi) & \pi \leqslant \theta \leqslant 2\pi \end{cases} \quad (5)$$

where I_m is the phase current amplitude.

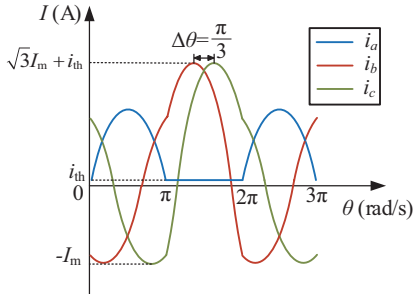

Fig. 14. Ideal three-phase current waveforms under fault-tolerant control.

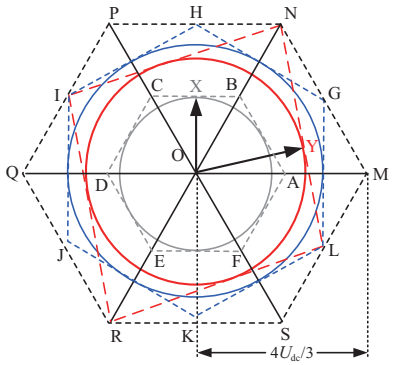

Fig. 15. Planar linear modulation range.

C. Linear Modulation Range Analysis

During fault-tolerant operation, ZSV is required in addition to the original command voltage in the *αβ*-plane. The ZSV can be considered the component in the zero axis. So, it is necessary to consider the linear modulation range based on the *αβ* plane and the zero axis simultaneously. In this section, the linear modulation range allowed with the proposed fault-tolerant modulation strategy is analyzed from the *αβ* plane and the zero axis respectively. According to the analysis in the previous section, when $i_a > i_{th}$, the middle vector combination is used for modulation, and the linear modulation range is the inscribed circle of the hexagon GHIJKL shown in Fig. 15. When $i_a < i_{th}$, the combination of middle vector and large vector is used for modulation, and the linear modulation range is the inscribed circle of the diamond IRLN shown in Fig. 15. Therefore, the linear modulation region on the *αβ* plane is the overlapping region of two inscribed circles, that is, the inscribed circle of the diamond IRLN, and its radius is $4U_{dc}/\sqrt{21}$.

Define the modulation index as:

$$m = \frac{\sqrt{21}\,|U_{ref}|}{4U_{dc}} \quad (6)$$

Equation (4) can be re-expressed as:

$$\begin{cases} T_1 = \dfrac{2\sqrt{7} m T_s}{7} \cos(\theta + \dfrac{\pi}{6}) \\ T_2 = \dfrac{3\sqrt{21} m T_s}{21} \sin(\theta + \dfrac{\pi}{6}) \end{cases} \quad (7)$$

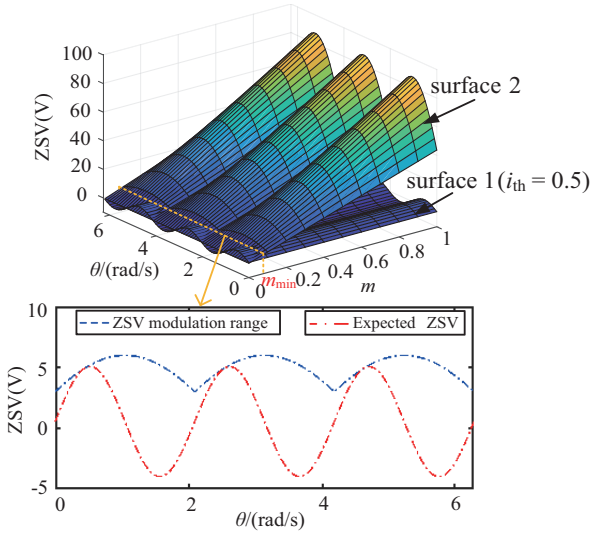

Fig. 16. Modulation range of ZSV.

Since i_a needs to be maintained at the threshold value i_{th} in the negative half cycle, the required ZSV in steady state is can be estimated as:

$$u_{0\text{inj}}^{*} = i_{th}R_0 + E_3 \sin(3\theta) \tag{8}$$

where R_0 is zero-sequence resistance, $E_3 = 3\omega\psi_{3f}$ represents the magnitude of zero-sequence electromotive force.

If phase-A current is small, in a switching period T_s, its value is all less than the set threshold current, then the positive ZSV injection modulation will be applied throughout the whole sampling period. In the sector I, the large voltage vector ON (25′) is the basic voltage vector injecting the positive ZSV, and the action time is T_2.Therefore, the ZSV in this sampling period can be calculated with

$$\begin{aligned} u_{0\text{out}} &= \frac{U_{dc}}{3}\frac{T_2}{T_s} \\ &= \frac{\sqrt{21}mU_{dc}}{21}\sin(\theta + \frac{\pi}{6}) \end{aligned} \tag{9}$$

Similarly, the ZSV values available in other sectors can be obtained by similar calculation, and the results are shown in Fig. 16. One can find that with the decrease of the modulation index m, the modulation range of the ZSV gradually decreases, and in each sector, it has the same maximum and minimum boundaries. The maximum output ZSV boundary in sector I is

$$(u_{0\text{out}})_{\max}\left|(T_1 = 0) = \frac{\sqrt{21}mU_{dc}}{21}\right. \tag{10}$$

And the minimum ZSV boundary in sector I is

$$(u_{0\text{out}})_{\min}\left|(T_1 = \sqrt{3}T_2) = \frac{\sqrt{21}mU_{dc}}{42}\right. \tag{11}$$

When the required injection ZSV intersects with the boundary of available ZSV, the minimum modulation index m satisfying the fault-tolerant operation requirement can be obtained as

$$m_{\min} = \frac{\sqrt{21}\left[i_{th}R_0 + E_{3\max}\sin(3\theta_i)\right]}{U_{dc}\sin(\theta_i + \frac{\pi}{6})} \tag{12}$$

where θ_i is the value of phase angle at the intersection point.

The intersection curve between the expected ZSV surface (surface 1) at i_{th} = 0.5 and the boundary of the ZSV modulation range surface (surface 2) is shown in Fig. 16, from which one can find that except for the critical point, the ZSV modulation range still has a sizable margin over the expected ZSV. In practice, considering the zero-sequence impedance is very small, the required ZSV is also small in voltage-second sense, it is not necessary to output the ZSV throughout the whole switching period. Therefore, the actual minimum modulation index is smaller than the theoretical value.

D. Output Performance Analysis

After the fault, the output performance of the OWEM driving system is limited by voltage and current. The voltage limit affects the speed range of the system, while the current limit decides the load capacity of the system.

Define the DC voltage utilization M as:

$$M = \frac{\sqrt{3}U_{lm}}{U_{dc}} \tag{13}$$

where U_{lm} is the maximum amplitude of the phase voltage that can be output in the linear modulation range.

In [11], the continuous two-phase fault-tolerant operation mode is adopted for fault-tolerant control. The synthesis of reference voltage vector is completed in the hexagonal ABCDEF region, and the linear modulation range is an inscribed circle with OX as its radius in Fig. 15. The maximum DC voltage utilization can be calculated by substituting $|\text{OX}| = U_{dc}/\sqrt{3}$ into (13) as 1. Similarly, from the analysis of the previous section, it has been found that the linear modulation range with the proposed fault-tolerant control strategy is the inscribed circle with OY as its radius in Fig. 15, and by substituting $|\text{OY}| = 4U_{dc}/\sqrt{21}$ into (13), one can find that the maximum DC voltage utilization is $4/\sqrt{7}$, which is 51.2% higher compared with the continuous two-phase fault-tolerant scheme.

The output range of the machine phase current can be used to evaluate the torque capability. Due to the asymmetry of the three-phase current after the fault, the rated root mean square (RMS) value is used to calculate the current value and the average torque is used to calculate the torque capability [17]. From (5), the RMS value of the current in phase A after fault is

$$\begin{aligned} I_{\text{af\_RMS}} &= \sqrt{\frac{1}{2\pi}\int_0^{\pi}(I_m \sin\theta)^2 \,\mathrm{d}\theta + i_{th}} \\ &\approx \frac{I_m}{2} = \frac{I_{\text{an\_RMS}}}{\sqrt{2}} \end{aligned} \tag{14}$$

where I_{an_RMS} and I_{af_RMS} are the root mean square values of phase-A current before and after the fault, respectively.

Similarly, the RMS values of the currents in phases B and C are

$$\begin{aligned} I_{bf\_RMS} &= \sqrt{\frac{1}{2\pi}\int_0^{\pi}\left[I_m \sin(\theta-\frac{2}{3}\pi)\right]^2 d\theta} \\ &+\sqrt{\frac{1}{2\pi}\int_{\pi}^{2\pi}\left[\sqrt{3}I_m \sin(\theta-\frac{5}{6}\pi)\right]^2 d\theta} \\ &= \sqrt{2}I_{bn\_RMS} \end{aligned} \tag{15}$$

$$I_{cf\_RMS} = \sqrt{2}I_{cn\_RMS} \tag{16}$$

Above analysis results indicate that under the premise that the given value of dq axis current is unchanged, the rated RMS value of the phase current after the fault can reach $\sqrt{2}$ times of that before the fault. Under the condition that the current is not overloaded, the average torque output capacity after the fault can be expressed as [17]:

$$T_{avef} = \frac{3}{2}\frac{P}{2}\lambda_{pm,d,dc},\ \frac{I_{xn\_RMS}}{\sqrt{2}} = \frac{T_{aven}}{\sqrt{2}} \tag{17}$$

where P is the number of poles, $\lambda_{pm,d,dc}$ is the average value of the d-axis permanent magnet flux, and I_{xn_RMS} is the rated RMS value of the machine phase current in the healthy operation.

Obviously, after the occurrence of a switch open-circuit fault, the torque output capacity is reduced to 0.707 times of that in the healthy state. In the continuous two-phase fault-tolerant operation mode, the torque output capability is reduced to 0.577 times of that in the healthy state, since the fault-phase current is constantly equal to 0. In comparison, the torque capacity with the proposed fault-tolerant strategy is increased by 22.5%.

IV. Experiments

To verify the effectiveness of the fault-tolerant control strategy proposed in this paper, a semi-physical simulation platform is built in a RT box, as shown in Fig. 17, with the machine parameters given in table I. The corresponding fault-tolerant control block diagram is shown in Fig. 18. The OWEM system model runs in RT Box, and the hardware circuit adopts DSP TMS320F28379D as the main control chip to run the control program. In the experiment, the DC voltage is set to 400 V, the PWM switching frequency is set to 10 kHz.

A. Fault-Tolerant Operation

Fig. 19 shows the experimental results of the OWEM system with a common DC bus without using any fault-tolerant control strategy in the case of a_{12} failure. The open-circuit fault of the switch device occurs at $t = 0.1$ s. As seen from the figure, the machine operates in a three-phase symmetrical operation state before the fault, and the three-phase current remains highly sinusoidal waveform. This verifies the effectiveness of

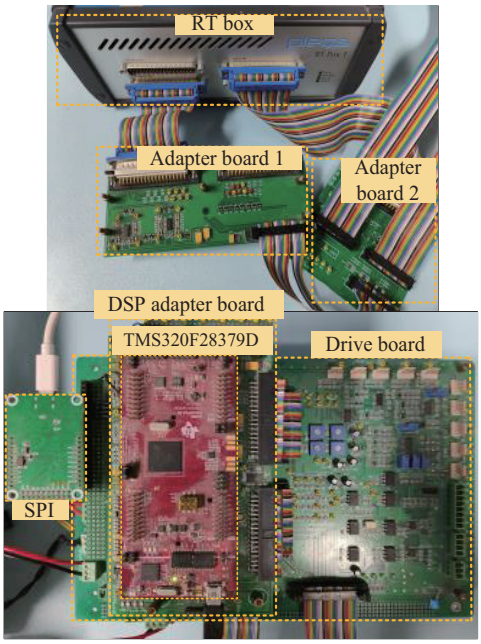

Fig. 17. Experimental platform.

TABLE I
Parameters of the OW-PMSM

Parameter	Value	Parameter	Value
rated power/kW	4	stator resistance/Ω	1.105
rated voltage/V	380	permanent magnetic flux/Wb	0.78
rated current/A	6.6	d-axis inductor/mH	45
rated frequency/Hz	50	q-axis inductor/mH	101
rated torque/N·m	20.1	number of pole pairs	2

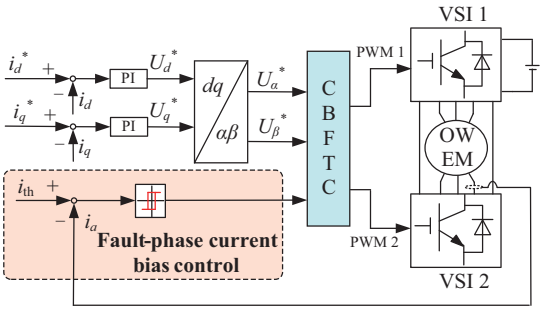

Fig. 18. Overall fault-tolerant control diagram.

the ZSC control, namely there is no obvious ZSC appearing in healthy operation state. As a result, the electromagnetic torque ripple is negligible. After the fault occurs, the negative half cycle of i_a is missing, and the remaining two-phase current are also distorted. The AC terminal of Bridge A in VSI 1 outputs an uncertain state in the negative half cycle, and obvious pulsations appear in the output torque of the machine. Besides, the ZSC suppression strategy fails in fault state due to selected switching combinations cannot be output effectively.

Fig. 20 shows the experimental results when using the continuous two-phase fault-tolerant control strategy presented

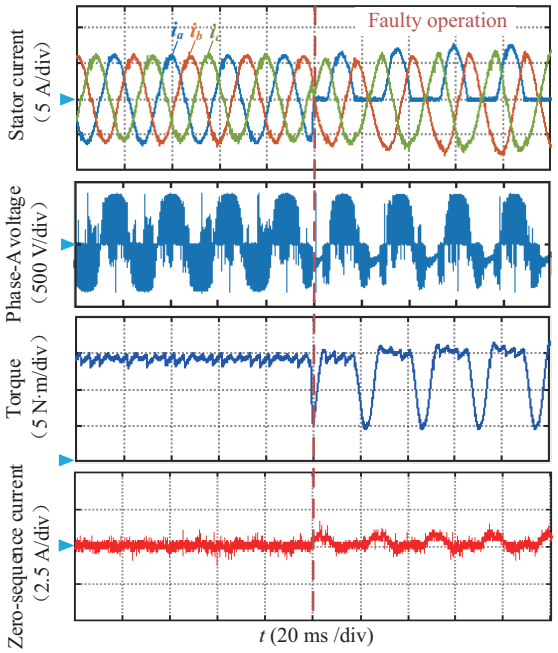

Fig. 19. Experimental results before and after failure without using any fault-tolerant control strategy.

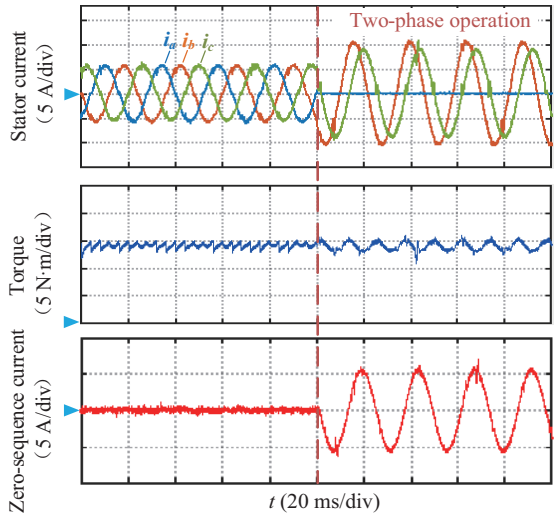

Fig. 20. Experimental results before and after failure using two-phase faulttolerant control strategy.

in [11] after a_{12} fault, where the switch fault occurs at t = 0.1 s. From the figure, it can be found that the fault-phase current ia drops to and maintains at 0 after the fault occurs. To maintain the magnetomotive force of the machine after the fault, the amplitude and phase of the currents flowing in the non-fault phases change accordingly. In the continuous two-phase operation mode, the electromagnetic torque still has a certain range of fluctuations and cannot be eliminated due to the possible freewheeling currents through the anti-diodes in phase A. Besides, the ZSC is high and equal to the sum of the phase-A and B currents. Due to the current limit, the torque capacity decreases significantly.

The experimental results adopting the proposed fault-

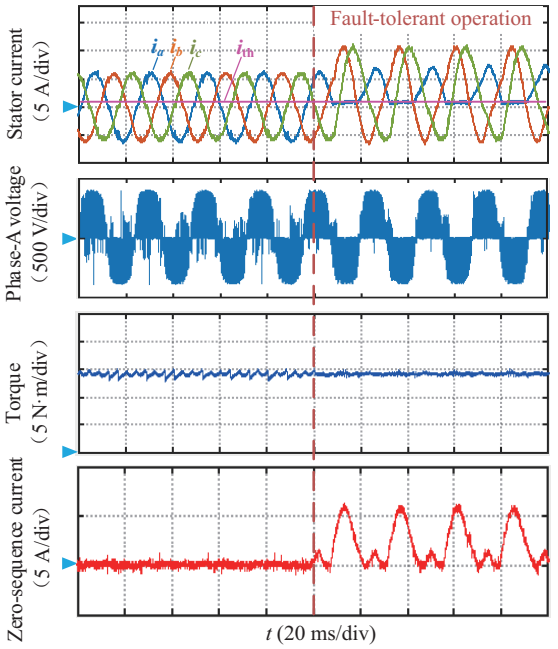

Fig. 21. Experimental results before and after failure using proposed fault-tolerant control strategy.

tolerant control strategy are shown in Fig. 21. As seen from the figure, the i_a is always higher than the threshold i_{th}, and the machine operates alternately between the two-phase mode and the three-phase mode, and the state at the AC terminal of Bridge A in VSI 1 is decisive throughout the fundamental period. Compared with Figs. 19 and 20, the torque ripple is significantly suppressed, and the ZSC is negligible in the positive half cycle, which provides current capability for torque output. It should be noted that in order to simplify the control, the ZSC is simply addressed by setting the ZSV due to the PWM itself equal to 0. However, the zero-sequence component of the electromotive force of the machine can also excite the ZSC. Therefore, the ZSC does not stay at 0 during the positive half cycle, as seen in Fig. 21. Fortunately, zero-sequence component is low, and consequently the current is also low. Therefore, the effects can be neglected. However, in theory it can be eliminated very well, if the ZSV is active control as in the healthy state rather than kept at 0. Though, this does not affect the effectiveness of the proposed fault-tolerant control strategy.

B. Fault-Tolerant Operation Performance in Steady State

To test the allowed speed range of the machine after a switch fault, comparative experiments under two-phase operation and fault-tolerant operation are made. Under two-phase operation mode, the motor is operated from low speed (ω_r = 10 rad/s) to high speed (ω_r = 157.1 rad/s), and the results are recorded in Fig. 22(a). From the figure, it can be find that the machine torque can be stably controlled at 12.5 N·m when the speed is below 130 rad/s. Once the speed exceeds 130 rad/s, the command voltage exceeds the maximum voltage range allowed by

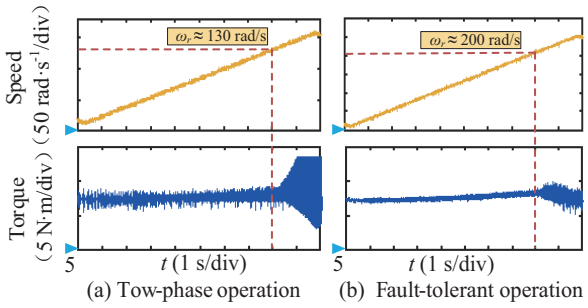

Fig. 22. Comparison of speed range under two-phase operation and fault-tolerant operation.

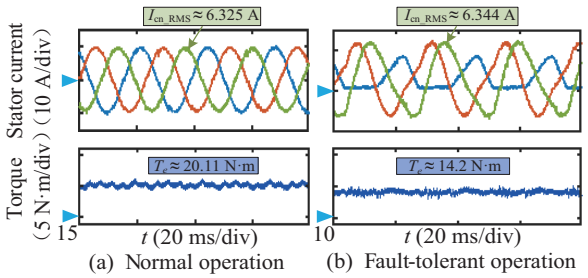

Fig. 23. Comparison of machine load capability under normal operation and fault-tolerant operation.

the two-phase control strategy, and the control system is gradually destabilized under the overmodulation. Fig. 22(b) shows the experimental results in the fault-tolerant operation mode, where the machine load is unchanged and the speed increases from 10 rad/s to a higher speed (ω_r = 251.3 rad/s). Obviously, the maximum speed allowed for the system to be stabilized is about 200 rad/s, which is 1.54 times of that under the two-phase operation mode. This shows that the machine still has a wide speed range with the proposed fault-tolerant control strategy in the paper, and which confirms the theoretical analysis on output voltage.

To evaluate the load capacity of the machine under fault-tolerant operation, comparative experiments under healthy and fault states are made. Under healthy condition, as shown in Fig. 23(a), the machine is operated at full load and normal speed (ω_r = 125.6 rad/s), and the torque is 20 N·m, i.e., the rated value. The RMS value of the phase-C current is 6.3 A, which is set as the rated RMS value of the phase current. In the fault operation, the machine is also operated at the same speed, as shown in Fig. 23(b). By increasing the load, the RMS value of the non-fault phase, here phase-C current is recorded, which reaches 6.3 A. The output torque at this time is approximately 14.2 N·m, which is 0.706 times of the rated torque in healthy operation. Through this experiment the analysis on voltage and torque capability during the fault operation is confirmed.

C. Performance in Transition and Dynamic Process

Fig. 24 shows the experimental waveforms of the drive system transiting from the healthy operation to the fault operation before the fault-tolerant strategy activated and to the fault operation with the fault-tolerant strategy activated. During this process the

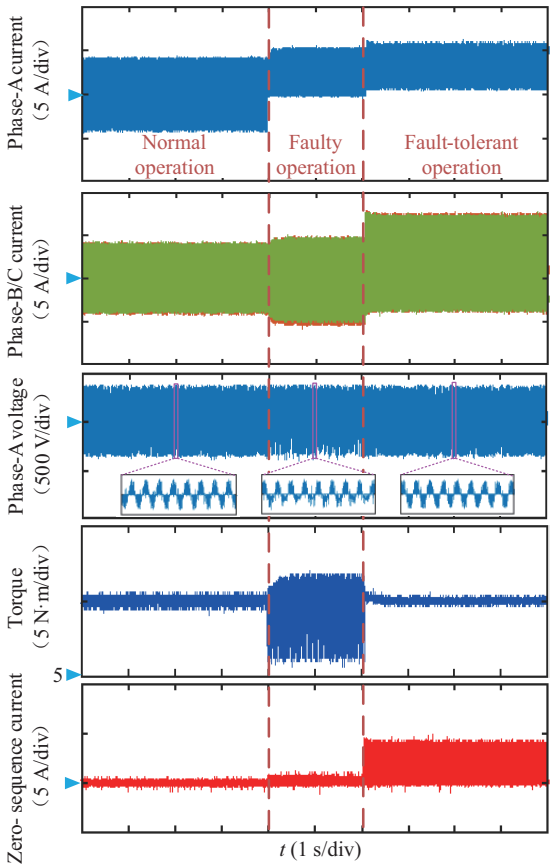

Fig. 24. Experimental results of dynamic transition process of three operating modes.

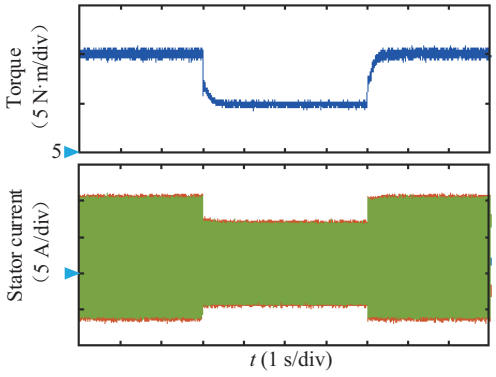

Fig. 25. Fault-tolerant effect during torque mutation process.

speed is set at 137.1 rad/s and the electromagnetic torque is equal to 10 N·m. At the time of t = 4 s, the switch device a_{12} fails, and the machine enters into the fault state operation but without any fault-tolerant control strategy adopted. At 6 s, the proposed fault-tolerant control strategy is activated. One can find that with the proposed scheme the transition is completed softly and easily.

Figs. 25 and 26 shows the operation results during the step response of electromagnetic torque and speed. In Fig. 25, the electromagnetic torque drops and rises sharply between 10 N·m and 15 N·m at t = 3 s and t = 7 s, respectively. And the speed

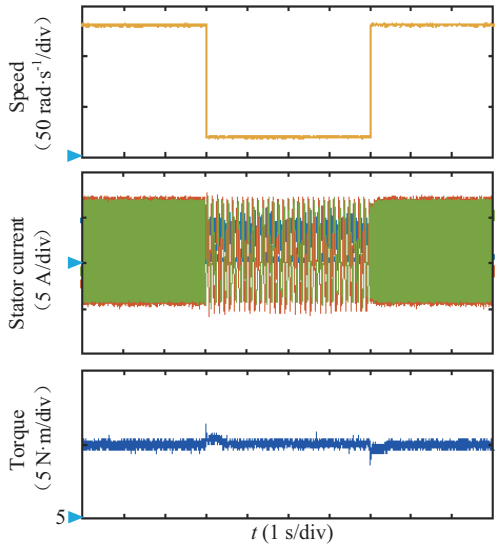

Fig. 26. Fault-tolerant effect during speed mutation process.

drops and rises sharply between 20 rad/s and 135 rad/s at t = 3 s and t = 7 s, as shown in Fig. 26. The torque assumes no obvious ripples during either sudden changes in torque or speed, that is to say, the proposed fault-tolerant control is still effective in these dynamic response processes.

V. Conclusion

In this paper, a fault-tolerant operation strategy is proposed for the OWEM with a common DC bus, based on fault phase current bias. Beneficial the freewheeling action of the anti-diode in the fault bridge, the desired output voltage can still be ensured. With this strategy, the machine operates in the two-phase mode and the three-phase mode alternatively. Compared with the fault-tolerant strategy operate the machine continuously at the two-phase mode, both the rated speeds and the load torque capability are increased 51.2% and 22.5%, which is crucial to vehicles.

References

[1] N. Chai and W. Hu, "A fault-tolerant scheme against the open-switch failure in open-end winding PMSM system with isolated DC bus," in *IEEE Transactions on Energy Conversion*, vol. 38, no. 3, pp. 2227–2230, Sept. 2023.

[2] K. Lee and Y. Han, "Simple discontinuous pulse-width modulation scheme for the loss reduction of a dual inverter fed an open-end winding induction motor," in *IEEE Transactions on Energy Conversion*, vol. 38, no. 1, pp. 495–506, Mar. 2023.

[3] T. M. Jahns and H. Dai, "The past, present, and future of power electronics integration technology in motor drives," in *CPSS Transactions on Power Electronics and Applications*, vol. 2, no. 3, pp. 197–216, Sept. 2017.

[4] F. Wu and J. Zhao, "Current similarity analysis-based open-circuit fault diagnosis for two-level three-phase PWM rectifier," in *IEEE Transactions on Power Electronics*, vol. 32, no. 5, pp. 3935–3945, May 2017.

[5] I. Jlassi, J. O. Estima, S. K. El Khil, N. M. Bellaaj, and A. J. M. Cardoso, "A robust observer-based method for IGBTs and current sensors fault diagnosis in voltage-source inverters of PMSM drives," in *IEEE Transactions on Industry Applications*, vol. 53, no. 3, pp. 2894–2905, May-Jun. 2017.

[6] C. Jiang, H. Liu, P. Wheeler, F. Wu, Z. Cai, and J. Huo, "A novel open-circuit fault detection and location for open-end winding PMSM based on differential-mode components," in *IEEE Transactions on Industrial Electronics*, vol. 69, no. 8, pp. 7776–7786, Aug. 2022.

[7] S. Yang, X. Sun, M. Ma, X. Zhang, and L. Chang, "Fault detection and identification scheme for dual-inverter fed OEWIM drive," in *IEEE Transactions on Industrial Electronics*, vol. 67, no. 7, pp. 6112–6123, Jul. 2020.

[8] K. Zhang, B. Gou, and X. Feng, "Online fault diagnosis for single-phase PWM rectifier using data-driven method," in *CPSS Transactions on Power Electronics and Applications*, vol. 7, no. 1, pp. 49–57, Mar. 2022.

[9] M. -A. Shamsi-Nejad, B. Nahid-Mobarakeh, S. Pierfederici, and F. Meibody-Tabar, "Series architecture for fault tolerant PM drives: Operating modes with one or two DC voltage source(s)," in *2010 IEEE International Conference on Industrial Technology*, Via del Mar, Chile, 2010, pp. 1525–1530.

[10] M. J. Duran and F. Barrero, "Recent advances in the design, modeling, and control of multiphase machines—Part II," in *IEEE Transactions on Industrial Electronics*, vol. 63, no. 1, pp. 459–468, Jan. 2016.

[11] K Yang, "Research of control system of three-phase open-end winding permanent magnet synchronous machine," Ph.D. dissertation, Dept. Elect. Eng., HIT., Harbin, China, 2016.

[12] W. Hu, C. Ruan, H. Nian, and D. Sun, "Simplified modulation scheme for open-end winding PMSM system with common DC bus under open-phase fault based on circulating current suppression," in *IEEE Transactions on Power Electronics*, vol. 35, no. 1, pp. 10–14, Jan. 2020.

[13] Y. Bao, X. Zhang, J. Zhao, B. Li, and C. Xu, "Research of fault-tolerant control strategy for open-end winding PMSM under open-phase fault," in *2023 IEEE PELS Students and Young Professionals Symposium (SYPS)*, Shanghai, China, 2023, pp. 1–5.

[14] J. A. Restrepo, A. Berzoy, A. E. Ginart, J. M. Aller, R. G. Harley, and T. G. Habetler, "Switching strategies for fault tolerant operation of single DC-link dual converters," in *IEEE Transactions on Power Electronics*, vol. 27, no. 2, pp. 509–518, Jan. 2012.

[15] C. Li, W. Huang, F. Bu, and J. Shao, "An open-end winding induction motor driver with boost and fault-tolerant function," in *Transactions of China Electrotechnical Society*, vol. 32, no. 5, pp. 97–104, Mar. 2017.

[16] I. Jlassi and A. J. M. Cardoso, "Fault-tolerant back-to-back converter for direct-drive PMSG wind turbines using direct torque and power control techniques," in *IEEE Transactions on Power Electronics*, vol. 34, no. 11, pp. 11215–11227, Nov. 2019.

[17] B. Zhu, C. Tan, M. Farshadnia, and J. E. Fletcher, "Postfault zero-sequence current injection for open-circuit diode/switch failure in open-end winding PMSM machines," in *IEEE Transactions on Industrial Electronics*, vol. 66, no. 7, pp. 5124–5132, Jul. 2019.

[18] W. Deng, J. Tang, and W. Cheng, "An enhanced rotating vector-based direct torque control for matrix converter-fed PMSM drives using virtual pulsating vectors," in *CPSS Transactions on Power Electronics and Applications*, vol. 8, no. 1, pp. 65–73, Mar. 2023.

[19] X. Lin, W. Huang, and L. Wang, "SVPWM strategy based on the hysteresis controller of zero-sequence current for three-phase open-end winding PMSM," in *IEEE Transactions on Power Electronics*, vol. 34, no. 4, pp. 3474–3486, Apr. 2019.

[20] R. Baranwal, K. Basu, and N. Mohan, "Carrier-based implementation of SVPWM for dual two-level VSI and dual matrix converter with zero common-mode voltage," in *IEEE Transactions on Power Electronics*, vol. 30, no. 3, pp. 1471–1487, Mar. 2015.

[21] A. Aghazadeh, M. Jafari, N. Khodabakhshi-Javinani, H. Nafisi, and H. Jabbari Namvar, "Introduction and advantage of space opposite vectors modulation utilized in dual two-level inverters with isolated DC sources," in *IEEE Transactions on Industrial Electronics*, vol. 66, no. 10, pp. 7581–7592, Oct. 2019.

[22] X. Zhang and C. Xu, "Second-time fault-tolerant topology and control strategy for the open-winding PMSM system based on shared bridge arm," in *IEEE Transactions on Power Electronics*, vol. 35, no. 11, pp. 12181–12193, Nov. 2020.

Zhongjie Zou received the B.S. degree in electrical engineering and automation from the School of Mechanical and Electrical Engineering, Anhui Jianzhu University, China, in 2017. He is currently pursuing the Master degree in electrical engineering at Hefei University of Technology. His current research interests include fault-tolerant control of open-end winding mechine.

Shuying Yang received the B.Sc. and Ph.D. degrees in automation and electrical engineering from Hefei University of the Technology (HFUT), Hefei, China, in 2002 and 2008, respectively. He joined the teaching faculty of the School of Electrical Engineering and Automation, HFUT, in 2005. From Aug. 2014 to Oct. 2015, he served as a visiting scholar at the University of New Brunswick, Canada. Now, he is a Professor with HFUT. His research interests and experience include renewable energy conversion, electric drive, and application of control theory.

Yufeng Zhang received the B.S. degree from Luoyang Institute of Science and Technology, Luoyang, China, in 2017 and M.S. degree from China University of Petroleum (East China), Qingdao, China, in 2021. He is currently pursuing the Ph.D. degree in electrical engineering at Hefei University of Technology. His research interest includes identification of broadband grid impedance.

Xing Zhang received the B.Sc., MA.Eng., and Ph.D. degrees in automation, automation, and electrical engineering from Hefei University of Technology (HFUT), Hefei, China, in 1984, 1990, and 2003, respectively. In 1984, he joined the teaching faculty of School of Electrical Engineering and Automation, HFUT, where he is currently a Professor and is also at the Photovoltaic Engineering Research Center of Ministry of Education, China. He is an Associate Editor for the *IEEE Journal of Emerging and Selected Topics in Power Electronics*. He has been cooperating with the Sungrow Power Supply Co., Ltd for a long time in the area of power electronics. His main research interests include photovoltaic generation technologies, wind power generation technologies, and distributed generation system.